CAMBRIDGE
UNIVERSITY PRESS

Research Article

Low-frequency pulse-jitter measurement with the uGMRT I: PSR J0437−4715

Tomonosuke Kikunaga[1,2], Shinnosuke Hisano[3], Neelam Dhanda Batra[4], Shantanu Desai[5], Bhal Chandra Joshi[6,7], Manjari Bagchi[8,9], T. Prabu[10], Keitaro Takahashi[11,3], Swetha Arumugam[12], Adarsh Bathula[13], Subhajit Dandapat[14], Debabrata Deb[8], Churchil Dwivedi[15], Yashwant Gupta[16], Shebin Jose Jacob[17], Fazal Kareem[18,19], K. Nobleson[20], Pragna Mamidipaka[12], Avinash Kumar Paladi[21], B. Arul Pandian[10,22], Prerna Rana[14], Jaikhomba Singha[23], Aman Srivastava[5], Mayuresh Surnis[24], and Pratik Tarafdar[8]

[1]Graduate School of Science and Technology, Kumamoto University, Kumamoto, Japan, [2]Australia Telescope National Facility, CSIRO Space and Astronomy, Epping, NSW, Australia, [3]International Research Organization for Advanced Science and Technology, Kumamoto University, Kumamoto, Japan, [4]Department of Physics and Astrophysics, Delhi University, Delhi, India, [5]Department of Physics, IIT Hyderabad, Kandi, Telangana, India, [6]National Centre for Radio Astrophysics (TIFR), Pune, India, [7]Department of Physics, Indian Institute of Technology, Roorkee, India, [8]The Institute of Mathematical Sciences, Taramani, Chennai, India, [9]Homi Bhabha National Institute, Training School Complex, Anushakti Nagar, Mumbai, India, [10]Raman Research Institute, Bangalore, India, [11]Faculty of Advanced Science and Technology, Kumamoto University, Kumamoto, Japan, [12]Department of Electrical Engineering, IIT Hyderabad, Kandi, Telangana, India, [13]Department of Physical Sciences, IISER Mohali, Punjab, India, [14]Department of Astronomy and Astrophysics, Tata Institute of Fundamental Research, Navy Nagar, Colaba, Mumbai, India, [15]Department of Earth and Space Sciences, Indian Institute of Space Science and Technology, Thiruvananthapuram, Kerala, India, [16]National Centre for Radio Astrophysics, Pune University Campus, Pune, India, [17]Department of Physics, Government Brennen College, Kannur University, Thalassery, Kannur, Kerala, India, [18]Department of Physical Sciences, IISER Kolkata, Mohanpur, West Bengal, India, [19]Center of Excellence in Space Sciences India, IISER Kolkata, Mohanpur, West Bengal, India, [20]International Research Organization for Advanced Science and Technology, Kumamoto University, Kurokami, Kumamoto, Japan, [21]Department of Physics, Indian Institute of Science, Bengaluru, Karnataka, India, [22]Christ University, Bangalore, India, [23]Department of Mathematics and Applied Mathematics, University of Cape Town, Cape Town, South Africa and [24]Department of Physics, Indian Institute of Science Education and Research Bhopal, Bhauri, Bhopal, Madhya Pradesh, India

Abstract

High-precision pulsar timing observations are limited in their accuracy by the jitter noise that appears in the arrival time of pulses. Therefore, it is important to systematically characterise the amplitude of the jitter noise and its variation with frequency. In this paper, we provide jitter measurements from low-frequency wideband observations of PSR J0437−4715 using data obtained as part of the Indian Pulsar Timing Array experiment. We were able to detect jitter in both the 300–500 MHz and 1 260–1 460 MHz observations of the upgraded Giant Metrewave Radio Telescope (uGMRT). The former is the first jitter measurement for this pulsar below 700 MHz, and the latter is in good agreement with results from previous studies. In addition, at 300–500 MHz, we investigated the frequency dependence of the jitter by calculating the jitter for each sub-banded arrival time of pulses. We found that the jitter amplitude increases with frequency. This trend is opposite as compared to previous studies, indicating that there is a turnover at intermediate frequencies. It will be possible to investigate this in more detail with uGMRT observations at 550–750 MHz and future high-sensitive wideband observations from next generation telescopes, such as the Square Kilometre Array. We also explored the effect of jitter on the high precision dispersion measure (DM) measurements derived from short duration observations. We find that even though the DM precision will be better at lower frequencies due to the smaller amplitude of jitter noise, it will limit the DM precision for high signal-to-noise observations, which are of short durations. This limitation can be overcome by integrating for a long enough duration optimised for a given pulsar.

Keywords: Radio astronomy; pulsars: individual: PSR J0437–4715; pulsar timing method

(Received 4 December 2023; revised 1 March 2024; accepted 30 March 2024)

1. Introduction

Pulsars are rapidly rotating neutron stars that emit beamed emission, which is observed as a pulsed signal. Among the different types of pulsars, millisecond pulsars (MSPs) have the most stable periods, making them the most precise clocks in the universe. The precise timing of MSPs has been used to search for nanohertz gravitational waves (GWs) by multiple consortia, known as Pulsar

Timing Arrays (PTAs) (Foster & Backer 1990), such as the North American Nanohertz Observatory for Gravitational Waves (McLaughlin 2013,NANOGrav), the European Pulsar Timing Array (Kramer & Champion 2013, EPTA), the Parkes Pulsar Timing Array (Hobbs 2013; Manchester et al. 2013, PPTA), the Indian Pulsar Timing Array (Joshi et al. 2018, 2022, InPTA), the Chinese Pulsar Timing Array (Lee 2016, CPTA) and the MeerTime Pulsar Timing Array (Bailes et al. 2020; Spiewak et al. 2022, MPTA). Recently, NANOGrav, EPTA+InPTA, PPTA, and CPTA announced evidence for nanohertz stochastic gravitational wave background (SGWB) with statistical significance ranging between $2 - 4\sigma$ (Agazie et al. 2023b; Antoniadis et al. 2023b; Reardon et al. 2023a; Xu et al. 2023). With the next generation, high-sensitivity telescopes, such as the Square Kilometre Array (SKA) it will be possible to obtain sufficient signal-to-noise ratio (S/N) within short observation duration to measure the pulse times of arrival (TOA). In the future, a large number of high cadence timing observations on a much larger pulsar sample will be made during the SKA era, which will lead to significant improvements in the sensitivity to detection of nanohertz GWs from the PTAs. This will not only facilitate the detection of SGWB at high confidence level, but will also open our horizon towards continuous GWs from individual supermassive black hole binaries, thereby ushering in the era of multi-wavelength GW astronomy.

In order to maximise the PTA sensitivity to GWs, a detailed characterisation of the different noise sources is of crucial importance. There are many noise sources that contribute to the uncertainty in the TOAs. Noise can be classified according to several characteristics, one of which is the temporal correlation. A noise with long-term correlation is called red noise. Some examples of red noise include rotational irregularities in the pulsar's spin period, also known as spin noise or timing noise (Boynton et al. 1972; Cordes 1980; Shannon & Cordes 2010), temporal variation in the Dispersion Measure (DM) caused by the interstellar plasma (Keith et al. 2013; Tarafdar et al. 2022), and errors in the Solar System ephemeris (Champion et al. 2010). On the other hand, noise without temporal correlation is called white noise. Another feature to classify the different sources of noise is their dependence on the observation frequency. While dispersive delays depend on the frequency, errors in the Solar System ephemeris are achromatic. Furthermore, whether a noise source is common to multiple pulsars or unique to each pulsar is of vital importance for distinguishing the GW signal from noise. The PTA experiments attempt to extract the GW signals by modelling these kinds of noise and incorporating them into their data analysis pipelines (Chalumeau et al. 2022; Srivastava et al. 2023; Agazie et al. 2023a; Antoniadis et al. 2023a; Reardon et al. 2023b). Although, many sources of noise are well understood both statistically and physically, there is room for further improvement in noise modelling.

Jitter noise refers to stochastic fluctuations in the pulsar timing residuals with a white noise spectrum and is one of the noise sources that should be characterised precisely to improve pulsar timing analysis. We, however, note that jitter is temporally correlated in the phase of the pulsar. The white noise spectrum also includes a contribution from the radiometer noise originating from the instrument. The amplitude of the radiometer noise depends on the instrument and this noise can be reduced, thereby improving the S/N ratio. On the other hand, jitter noise does not decrease, even if the S/N ratio improves and its amplitude is independent of the instrument (Shannon & Cordes 2012; Shannon et al. 2014; Lam et al. 2016). Furthermore, radiometer noise is always uncorrelated in time (barring instrumental issues)

and homoscedastic across the pulse phase, while jitter is both correlated and heteroscedastic (Osłowski et al. 2011). Hence, this noise is considered intrinsic to each pulsar, and it occurs due to pulse shape variations on pulse-to-pulse scale. Since it behaves like white noise, its amplitude decreases with an increase in the integration time. However, with the shorter duration of observations, which are likely to be planned for the next generation PTA experiments due to their higher sensitivity, these experiments may suffer from jitter noise, if its implications are not understood properly. Therefore, it is important to investigate the nature and amplitude of the jitter noise with current observational campaigns in order to develop efficient observation strategies for the future.

For this work, we study the jitter noise in the pulsar PSR J0437−4715. This pulsar was discovered in the Parkes 70 cm survey and is the brightest known MSP (Johnston et al. 1993). Due to its high brightness, it has been extensively studied especially for its single-pulse behaviour. (Ables et al. 1997; Jenet Q5 et al. 1998;Vivekanand et al. 1998;Vivekanand 2000; Liu et al. 2012; Osłowski et al. 2014; De et al. 2016).

This pulsar has also been the focus of previous jitter studies, which measured its jitter amplitude at different frequencies (Shannon et al. 2014; Parthasarathy et al. 2021, hereafter S14 and P21, respectively). S14 measured its jitter amplitude using 700, 1 400, and 3 100 MHz observations by the Parkes *Murriyang* telescope, whereas P21 investigated the wideband feature of its jitter using the MeerKAT telescope (856–1 712 MHz). Both studies found that the jitter amplitude of PSR J0437−4715 has a weak frequency dependence, and its amplitude is larger at lower frequencies. PSR J0437−4715 has been subsequently observed by PPTA, MPTA, and InPTA, since it is located in the southern sky. Among these three PTAs, only InPTA covers the low-frequency range (300–500 MHz). Therefore, we are the only PTA, which can investigate whether the jitter amplitude of PSR J0437−4715 is actually getting larger in the lower frequency bands, and this investigation has important ramifications for developing a future strategy for low-frequency timing observations.

In this paper, we report the pulse jitter measurements of PSR J0437−4715 for low (300–500 MHz) and mid (1 260–1 460 MHz) radio frequency observations using the upgraded Giant Metrewave Radio Telescopeu (GMRT). The rest of this paper is structured as follows: In Section 2, we briefly describe the observations used in this work and the data processing methods used for analysis. In Section 3, we describe the methodology used for estimating jitter noise and the results of these measurements. In Section 4, we discuss the inferences and conclusions made from our analysis. Finally, we summarise our findings and conclude in Section 5.

2. Observations and data processing

2.1. Observations

In this work, we have used the observations of PSR J0437−4715 conducted using uGMRT (Gupta et al. 2017) as a part of the InPTA experiment from the observation Cycle 41 to 44 (October 2021 to September 2023). The InPTA observations were carried out either using two sub-arrays of 10–15 antennae at Band 3 (300–500 MHz) and Band 5 (1 260–1 460 MHz), respectively or using the complete array set at Band 3. The voltages from individual antennas were added after compensating for the phase difference between different antennas to form phased array beams for both Band 3 and Band 5. This Nyquist sampled time series was converted to 1

Table 1. Band 3 observations used in this work and their estimated jitter amplitudes. The first column lists the uGMRT observation cycle. The second column shows the date of the observations. The third column gives the integrated S/N ratios for this band obtained from the `pdmp` command of `PSRCHIVE` software package. The fourth column is the observation duration in seconds. The last column shows the ECORR value scaled to one hour and these values are plotted in Fig. 5. The bottom six epochs were selected to see the difference between Band 3 and 5 for the same epochs (see Section 3.3).

Cycle	MJD	S/N	Duration (s)	ECORR (ns)
41	59545	16 401	1 198	$63.36^{+4.53}_{-4.23}$
41	59587	8 667	1 799	$64.84^{+4.64}_{-4.33}$
41	59627	7 571	1 018	$53.06^{+3.38}_{-3.12}$
41	59656	6 602	1 020	$64.32^{+5.04}_{-4.49}$
41	59665	4 772	1 320	$47.79^{+4.25}_{-3.93}$
42	59692	5 196	719	$68.48^{+6.51}_{-5.64}$
42	59701	14 708	720	$52.70^{+5.08}_{-4.64}$
42	59730	10 452	718	$52.04^{+4.90}_{-4.35}$
42	59789	13 307	718	$59.32^{+5.78}_{-4.95}$
42	59800	11 717	718	$64.58^{+5.85}_{-5.16}$
43	59908	12 651	598	$52.70^{+3.77}_{-3.52}$
43	59918	10 150	720	$31.76^{+3.06}_{-2.79}$
43	59928	13 041	597	$47.86^{+5.20}_{-4.51}$
43	59989	11 379	660	$53.05^{+5.26}_{-4.57}$
43	60021	18 320	1 496	$52.98^{+3.43}_{-3.09}$
44	60063	5 487	600	$52.07^{+6.08}_{-5.29}$
44	60121	12 228	598	$56.33^{+5.85}_{-5.04}$
44	60139	6 250	600	$49.49^{+5.56}_{-4.78}$
44	60160	13 017	598	$68.70^{+7.01}_{-6.04}$
44	60178	23 971	600	$50.24^{+5.18}_{-4.38}$
41	59575	2 596	1 318	$63.19^{+6.20}_{-5.86}$
42	59818	2 627	719	$53.93^{+6.58}_{-5.87}$
43	59982	5 265	900	$49.72^{+4.81}_{-4.25}$
43	60002	6 942	720	$61.90^{+6.40}_{-5.73}$
44	60055	4 930	900	$55.58^{+5.37}_{-4.87}$
44	60149	5 211	720	$53.54^{+5.45}_{-4.77}$

Table 2. Band 5 observations used in this work. The different columns refer to same parameters as in Table 1.

Cycle	MJD	S/N	Duration (s)	ECORR (ns)
41	59545	1 253	1 215	$61.92^{+4.43}_{-4.13}$
41	59565	1 126	1 034	$56.47^{+6.89}_{-7.29}$
41	59575	1 647	1 334	$61.92^{+5.97}_{-5.45}$
41	59627	1 465	1 033	$57.15^{+7.24}_{-6.91}$
41	59665	1 332	1 345	$66.51^{+6.94}_{-6.40}$
42	59692	1 431	734	$58.28^{+7.01}_{-6.22}$
42	59782	938	733	$46.57^{+9.43}_{-9.86}$
42	59810	1 044	733	$49.33^{+8.60}_{-8.36}$
42	59818	1 696	734	$43.84^{+5.35}_{-4.77}$
42	59838	2 115	734	$56.47^{+5.45}_{-4.97}$
43	59898	1 237	720	$61.92^{+7.56}_{-6.73}$
43	59918	1 328	720	$64.90^{+10.15}_{-9.65}$
43	59959	730	901	$54.66^{+10.68}_{-11.01}$
43	59982	851	901	$61.92^{+7.56}_{-6.73}$
43	60002	812	721	$42.02^{+12.08}_{-20.46}$
44	60055	954	901	$60.28^{+8.91}_{-8.23}$
44	60149	1 470	722	$50.93^{+6.76}_{-6.14}$
44	60191	1 450	720	$52.17^{+6.43}_{-5.77}$

2.2. Data processing

The processing of uGMRT pulsar observations was done using publicly available pulsar analysis tools described in this section. Here, we briefly summarise the data processing steps involved and the relevant software that was used in the analysis. The raw spectral time series was first reduced by converting it into RFI-mitigated partially folded profiles averaged every 10 s for each frequency channel using `pinta`[a] (Susobhanan et al. 2021) pipeline. The steps involved are as follows:

1. Convert the raw spectral data to filterbank format after removing impulsive and periodic RFI using algorithms developed for the uGMRT data with `RFIClean`[b] (Maan et al. 2021), which automatically remove periodic RFI in the Fourier domain.

2. The RFI-mitigated filterbank data were then folded for every frequency channel using an updated ephemeris of the pulsar every 10 s. This was done in the pipeline using DSPSR[c] (van Straten & Bailes 2011). Each profile folded every 10 s represents a sub-integration in the observations consisting of all frequency channels that are recorded (128 and 1 024 in Band 3 and 5, respectively). These partially folded profiles were then written in the standard PSRFITS format for subsequent manipulation.

More details can be found in Susobhanan et al. (2021) (and references therein). The pipeline parameters used are listed in Table 3. The subsequent analyses used tools provided by PSRCHIVE[d] software package (Hotan et al. 2004; van Straten et al. 2012). For each epoch, an optimised S/N was obtained using the

024 frequency channels for Band 5 by taking a 2 048 point discrete Fourier Transform in the GMRT wideband backend. The Band 3 data were coherently dedispersed with the known DM of the pulsar to 128 frequency channels using a real-time pipeline (De & Gupta 2016) and sampled every 5.12 μs. As the dual-band observation mode with the uGMRT allows the coherent dedispersion pipeline to be used only at one of the bands, the spectral time series was recorded with 1 024 channels for Band 5, in the regular phased array mode and sampled every 40.96 μs. Given the low DM (2.6 pc cm^{-3}) of the pulsar, the dispersion smear across a Band 5 channel is much smaller ($\sim$2 μs) than the sampling time used for Band 5, which is approximately equal to a phase bin across the profile. Thus, we do not expect significant aliasing to affect our results despite our observations being limited by the allowed observing mode and the lack of coherent dedispersion. The Julian dates and S/N ratio for each epoch used for our analysis can be found in Tables 1 and 2 for Band 3 and Band 5, respectively. More details about the InPTA observations and the associated observing strategy can be found in Tarafdar et al. (2022) and Joshi et al. (2022).

[a]https://github.com/inpta/pinta.
[b]https://github.com/ymaan4/RFIClean.
[c]https://dspsr.sourceforge.net.
[d]https://psrchive.sourceforge.net/index.shtml.

Table 3. Parameters used in `pinta` reduction. The first column is the local oscillator frequency of the observing band. The second column is the number of phase bins. The third column is the number of frequency channels. The fourth columns denotes the observation bandwidth. The fifth column is the sampling time used for observation. The sixth column is the sideband. The seventh column is number of polarisations. The eighth column is the duration of individual sub-integrations. The last column is whether the data has been coherently dedispersed (1) or not (0). More details on the description of these parameters can be found in Susobhanan et al. (2021).

Parameters	Frequency (MHz)	N_{bins}	N_{chan}	Band width (MHz)	T_{smpl} (μs)	Sideband	N_{pol}	T_{subint} (s)	Coheded
Band 3	500	1 024	128	200	5.12	LSB	1	10	1
Band 5	1 460	128	1 024	200	40.96	LSB	1	10	0

`pdmp` command provided by `PSRCHIVE`. The resulting S/N values were used for selecting the optimal observations analysed in this paper. We selected five epochs from each cycle for both Band 3 and Band 5, except for Band 5 in Cycle 44, since we did not have enough high S/N epochs. We also analysed six additional epochs, which have moderate S/N ratio in Band 3, and which were already selected for Band 5, to check the difference between Band 3 and 5 in the same epoch. In total, we analysed 26 epochs for Band 3 and 18 epochs for Band 5 as listed in Tables 1 and 2, respectively.

We first collapsed all the frequency channels in each PSRfits file into eight sub-bands after de-dispersing them, using the `pam` command of `PSRCHIVE`. Here, `pam` (which stands for Pulsar Archive Manipulator) is one of the commands within `PSRCHIVE`, which is widely used for post-processing partially folded profiles, such as dedispersion, collapsing the data over frequency and time and modifying the meta-data in the PSRFITS header. Next, the time-of-arrival (ToA) for each partially folded profile was obtained by cross-correlating these with a frequency resolved template. The template was formed by averaging all the sub-intergations using `pam` while preserving the eight sub-bands. These time-collapsed data were then dedispersed to obtain a final noise-free template using a wavelet filter implemented in `psrsmooth` command of `PSRCHIVE`. ToAs for every sub-integration in each observations were then obtained by cross-correlating the partially folded profiles with the noise-free template using the `pat` command of `PSRCHIVE`.

Finally, we obtained the timing residuals using the `TEMPO2`[e] software packages for further analysis described in the next section. `TEMPO2` is a package for pulsar timing analysis. This software compares the observed ToA with that predicted from a timing model, consisting of rotational, astrometric and binary parameters of a pulsar (Hobbs et al. 2006; Edwards et al. 2006). The sum of squares of the differences between the observed and predicted ToAs, called timing residuals, is minimised to obtain the best fit parameters of the pulsar. `TEMPO2` is also used for simulating the ToAs using plug-ins provided in the software. We used `TEMPO2` for simulations to estimate pulse jitter as explained in the next section. Before proceeding with the jitter measurements, we removed the ToAs with large uncertainties from a visual check. Finally, we carried out parameter fitting using only the spin frequency and DM, since the observations typically span 10 minutes in duration.

3. Jitter measurements

In this section, we first describe the noise models and the methods used to measure the jitter amplitudes. Thereafter, we present the results of jitter measurements.
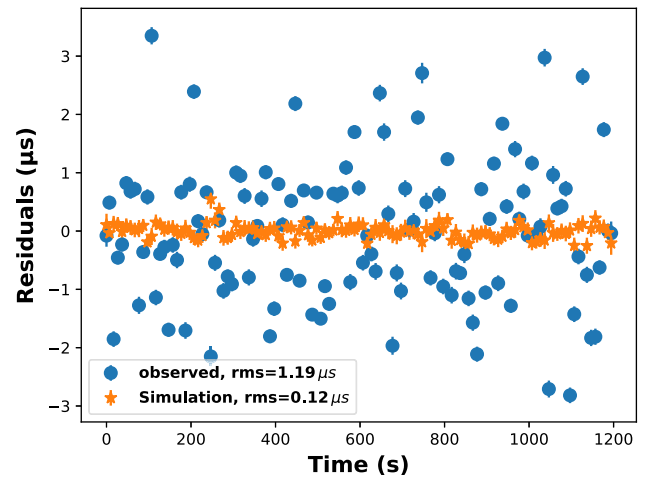

Figure 1. An example of the frequency-averaged timing residuals. The blue circles and orange stars denote the observed residuals obtained from 10 s sub-integrated profiles and residuals obtained with `libstempo` simulation, respectively (see the beginning of Section 3). The TOAs are obtained from Cycle 41 Band 3 observations for MJD 59545.

Traditionally, the jitter amplitudes have been estimated by computing the quadrature difference of the root-mean-square (rms) of frequency-averaged residuals, σ_{obs} and the rms expected from the radiometer noise, (σ_{rad}):

$$\sigma_J^2(T) = \sigma_{obs}^2(T) - \sigma_{rad}^2(T), \tag{1}$$

where T is the length of a sub-integration. We can estimate σ_{rad} by considering the Gaussian noise expected from the observed TOA uncertainties. The simulated TOAs can be obtained using the `fakepulsar` method from the `libstempo`[f] package, with the frequency-averaged TOAs and errors as input. `fakepulsar` is a plug-in within the `TEMPO2` package. This particular plug-in enables the user to create simulated TOAs that fit a given timing model in the form of a given parameter file (Hobbs et al. 2006). The timing model may correspond to either a real or a hypothetical pulsar. The addition of red and white noise is possible in this plug-in. The simulated timing residuals are encoded in an array with the same length as the total number of TOAs, which is filled with zeros. Then we can obtain the timing residuals containing radiometer noise by adding Gaussian noise using `add_efac` option. The rms of the timing residuals is denoted by σ_{rad}. We obtain σ_{rad} with 1 000 realisations and then calculate the jitter amplitude σ_J using Equation (1). One example of the frequency-averaged timing residuals and the simulated residuals is shown in Fig. 1. We can see that the frequency-averaged timing residuals

have large fluctuations compared to the simulated timing residuals, suggesting that the remaining TOA fluctuation is due to pulse jitter. Jitter noise behaves like a white noise source and hence its amplitude scales inversely with the square root of the integration time, as shown below.

$$\sigma_J(T_1) = \sigma_J(T_2)\sqrt{T_2/T_1} \quad (2)$$

For the rest of the paper, we report the jitter amplitudes, after rescaling them to 1 hour for the ease of comparison with previous studies.

3.1. Noise model

For the purpose of this study, we use Bayesian inference to estimate the jitter amplitude and used the traditional method described in the beginning of this section for crosscheck. In this subsection, we briefly describe the noise model used to estimate the jitter amplitude in this work. The following description is based on previous works (Lentati et al. 2014; van Haasteren & Vallisneri 2014; Arzoumanian et al. 2015; Srivastava et al. 2023), where more details can be found.

The observed timing residuals can be defined in terms of an N_{TOA} length vector, where $N_{\mathrm{TOA}} = N_{\mathrm{subint}} \times N_{\mathrm{subband}}$ for a given observation, and can be modelled as a sum of various deterministic and stochastic noise sources. Since we are interested in the stochastic noise within a single epoch, we assume that the timing residual vector (δt) can be fully described by the white noise term after removing the deterministic term. Therefore, the likelihood function can be written as follows:

$$L(\delta \mathbf{t}|\theta) = \frac{1}{\sqrt{(2\pi)^{N_{\mathrm{TOA}}} \det(\mathbf{C}(\theta))}} \exp\left(-\frac{1}{2}\delta \mathbf{t}^T \mathbf{C}(\theta)^{-1} \delta \mathbf{t}\right), \quad (3)$$

where $\mathbf{C}(\theta)$ is the covariance matrix and θ is a set of parameters.

In pulsar timing analysis, there are three parameters that are used to characterise white noise: EFAC, EQUAD, and ECORR. EFAC is a multiplicative scale factor that corrects for the underestimation of the TOA uncertainty that may be due to errors in calibration. EQUAD is a term that adds white noise in quadrature to represent the range of fluctuations beyond the TOA uncertainty. ECORR is similar to EQUAD, where white noise is again added in quadrature, but ECORR is uncorrelated in different time bins, but perfectly correlated at different frequencies. It represents the fluctuation of the TOA due to pulse profile variation. Therefore, ECORR corresponds to the jitter noise. EQUAD also corresponds to jitter as far as a single sub-band TOA is concerned. In this work, we use EFAC and EQUAD, when we estimate the jitter amplitude for each sub-banded TOA, and use EFAC and ECORR from the whole set of TOAs. We used the following three models to estimate the jitter amplitude:

Model I common EFAC and ECORR throughout the band.

Model II common EFAC throughout the band and different EQUAD for each sub-band.

Model III different EQUAD for each sub-band without EFAC.

In Model I, ECORR corresponds to the jitter amplitude for the given band. In Model II and III, we estimate the jitter for each sub-band. The aim of Model III is to eliminate any correlation between

the sub-bands, since we used a common EFAC in Model II. The covariance matrix for each model can be written as follows:[g]

$$\textbf{Model I} \quad C_{ij} = F^2 \sigma_{\mathrm{TOA},i}^2 \delta_{ij} + J^2 \delta_{t_i,t_j} \quad (4)$$

$$\textbf{Model II} \quad C_{ij} = \left(F^2 \sigma_{\mathrm{TOA},i}^2 + Q_{\nu_i}^2\right)\delta_{ij} \quad (5)$$

$$\textbf{Model III} \quad C_{ij} = \left(\sigma_{\mathrm{TOA},i}^2 + Q_{\nu_i}^2\right)\delta_{ij} \quad (6)$$

where $\sigma_{\mathrm{TOA},i}$ is the uncertainty of the ith TOA. F, J refer to EFAC and ECORR, respectively. Q_{ν_i} denotes EQUAD for the ith sub-band. The index t_i represents the sub-integration of the ith TOA to incorporate ECORR in the same sub-integration. We used uniform prior distribution in [0.5, 5.0] for EFAC and log-uniform prior distribution in [-10.0, -5.0] for EQUAD and ECORR.

3.2. Data analysis

To measure the jitter amplitude using Bayesian inference, we used the libstempo and the ENTERPRISE python packages (Ellis et al. 2020). libstempo is a Python wrapper to the tempo2 package. ENTERPRISE is a pulsar timing analysis software for pulsar noise analysis, GW searches and pulsar timing model analysis. We used the sub-banded TOAs and the corresponding par file as input. We then define the likelihood function depending on the Model I-III, from which the noise parameters are then estimated. We used the Markov Chain Monte Carlo (MCMC) sampler implemented in the PTMCMCSampler package (Ellis&van Haasteren 2017) to sample the posterior and estimate the EFAC and ECORR or EQUAD. PTMCMCSampler is an acronym for Parallel Tempering Markov Chain Monte Carlo sampler and utilises an adaptive jump proposal mechanism by default, incorporating both standard and single-component Adaptive Metropolis (AM) as well as Differential Evolution (DE) jumps. Moreover, MPI (mpi4py) is employed to execute the parallel chains in this implementation. One example of such a posterior plot along with the marginalised posteriors for EFAC and ECORR is shown in Fig. 2.

As mentioned at the beginning of Section 3, we rescale the estimated values of EQUAD and ECORR to one hour duration, using the same scaling relation as in Equation (2). However, in order to reaffirm whether they would follow the same relation as Equation (2), we recalculate ECORR for Model I by changing the sub-integration time to 20 and 40 seconds. The result is shown in Fig. 3, and we confirm that ECORR also follows the correct scaling law in accord with Equation (2). Although we do not have data for observation durations longer than one hour, we assume that the scaling law would hold even if the integration time is extended to one hour. Therefore, we scaled the jitter amplitude obtained by Bayesian analysis to one hour for ease of comparison with previous studies.

As a consistency check, we also verify whether the ECORR values obtained with ENTERPRISE are consistent with the jitter amplitude obtained with the traditional method described in the beginning of this section (see Fig. 4). We find that all the σ_J values agree with the ECORR values to within 1σ, thereby showing that our results are self-consistent.

---

[g]In the modern definition of EQUAD, EQUAD is defined with EFAC multiplied, but since we are interested in measuring the jitter amplitude in Equation (1) within a Bayesian framework, we adopt the definition of temponest without EFAC applied.
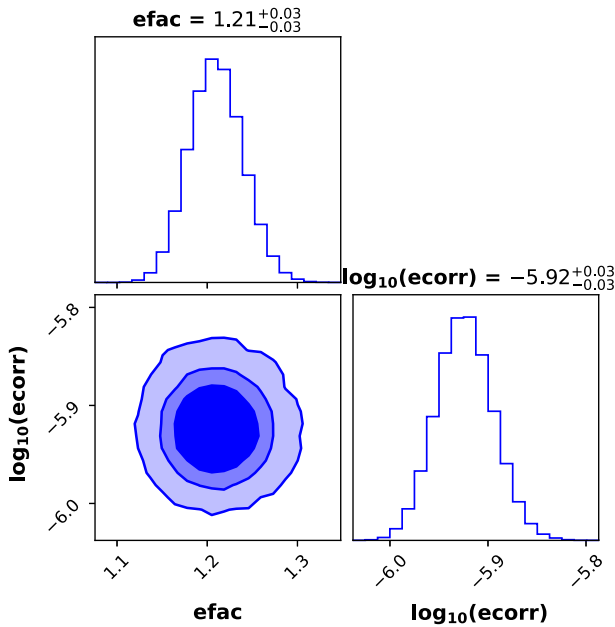
Figure 2. An example of the posterior distribution with 68%, 90%, 99% credible intervals of the Model I parameter estimation. The point estimates shown above the plots represent the median values and marginalised 68% credible intervals. The TOAs are obtained from Cycle 41 Band 3 observations on MJD 59545.
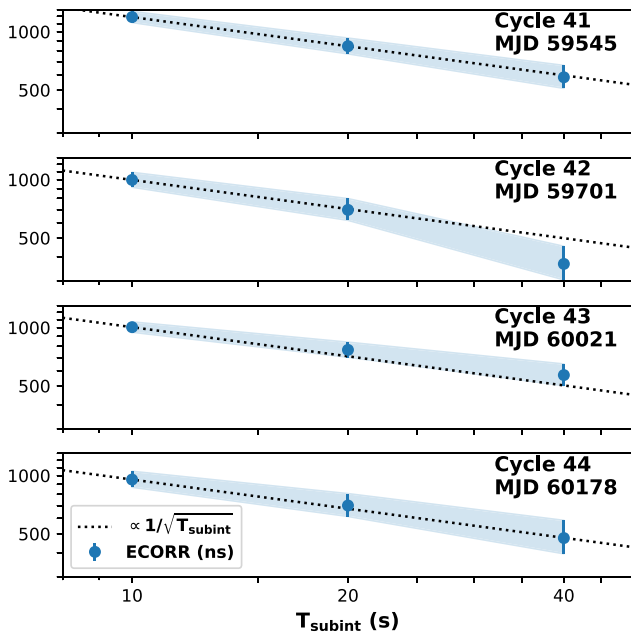

Figure 3. ECORR obtained with different sub-integration. Blue circles denote the ECORR values obtained from different sub-integration times. The black dotted lines shows the fit, which is proportional to the inverse square root of the sub-integration times.

3.3. Jitter amplitude within the band

Using the TOAs obtained by the method described in Section 2.2, we obtained ECORR values for all the selected epochs which are listed in Tables 1 and 2, for Model I of Section 3.1, which considers ECORR as a proxy for the jitter amplitude throughout the band.
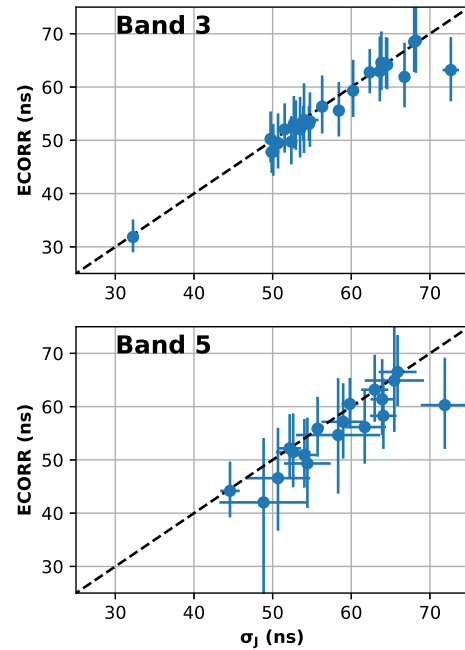
Figure 4. Comparison of jitter amplitudes obtained from Bayesian analysis and traditional method. The blue points denote jitter amplitude. The dashed black line represents the straight line given by $y = x$. All values are scaled to 1 hour value using Equation (2).

The resulting values of ECORR are rescaled to one hour and are listed in column 5 of Tables 1 and 2.

The rescaled ECORR values are plotted in Fig. 5 for each epoch. We estimate the weighted average of ECORR to be 53.2 ± 0.9 ns in Band 3 and 56.2 ± 1.6 ns in Band 5 from our observations. We find that our Band 5 result is consistent with P21. The jitter amplitude in S14 was reported for a single observation only. Though our weighted average value for Band 5 differs from that quoted in S14, the spread in our overall results ensures that we are in good agreement with S14 as well.

Our results for ECORR at Band 3 are the first jitter measurements calculated for PSR J0437−4715 below 700 MHz. Therefore, we do not have previous studies to directly compare our results. The frequency dependence suggested by S14 and P21 point to a higher jitter at lower frequencies. The results we derive are, however, not in agreement with this conclusion since we find that ECORR at Band 3 is consistent with that seen in Band 5. Also, we see that the weighted average of the jitter amplitude at Band 3 is slightly lower than that of Band 5. We calculated the weighted average again after excluding the epoch corresponding to MJD 59918, since it is likely to be an outlier as it is strongly affected by scintillation. This gave a new weighted average value of jitter at Band 3, equal to 55.47 ± 0.94 ns. Therefore, even after removing the outlier, the jitter in Band 3 is consistent with that in Band 5 within 1σ. One possible reason that the jitter in Band 3 is not so large could be due to epoch to epoch variations, since we are comparing different epochs. In Fig. 6, we plot the ECORR values for Band 3 and Band 5 from same epochs, for comparing their behaviour. We see that while there are some epochs where the jitter in Band 3 is larger, there are also epochs where the jitter values at Band 3 are the same or smaller. From our whole band jitter (ECORR) estimates, we conclude that it is not possible to say with
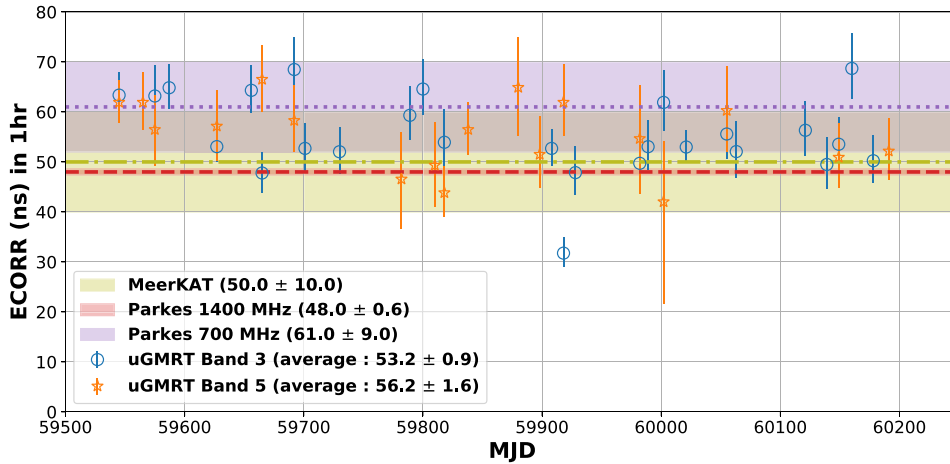
Figure 5. ECORR time series scaled to one hour obtained from Model I estimation. The blue circles and orange stars denote the ECORR values obtained from Band 3 and Band 5 observations, respectively. The purple shaded region and the dotted line show the results of MeerKAT observations (P21). The red shaded region and the dashed line and the yellow shaded region and dot-dashed line show the corresponding results for the Parkes observations (S14). Note that the values shown in the previous studies are not ECORR, but σ_J defined by the Equation (1), which is measured by the traditional method described in the beginning of Section 3.
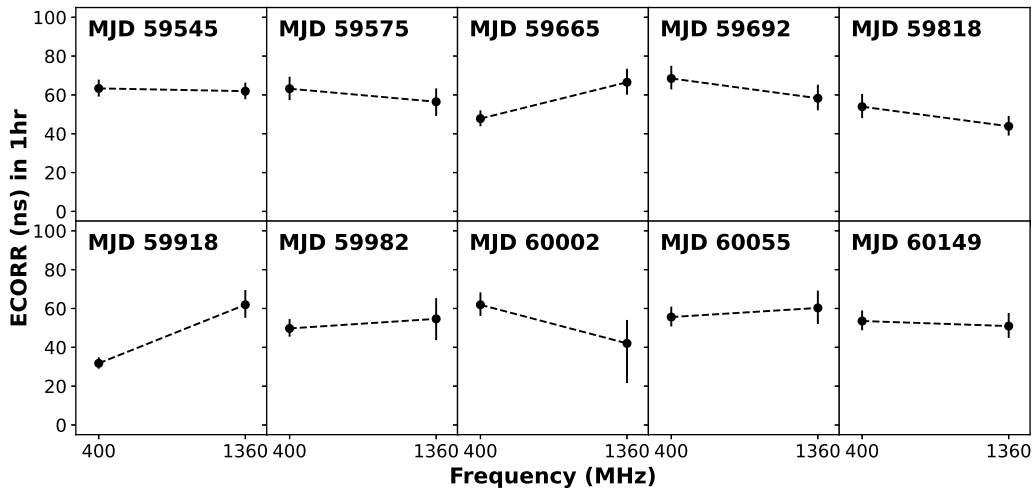
Figure 6. Comparison plots of ECORR for Band 3 and Band 5 for the same epoch obtained from Model I estimation.

certainty whether the jitter is larger or smaller at lower frequencies than at higher frequencies.

We see that there is a large scatter in the Band 3 jitter estimates. On investigating the Band 3 pulsar profiles in the frequency domain, we find that this scatter in the jitter values might be caused by the scintillation present in many profiles. Further, we notice that in this band, the S/N varies significantly with frequency as well as from epoch to epoch, which again can possibly be explained by the presence of interstellar scintillation in the data. This may have caused the failure in measuring the fluctuations of the timing residuals for some of the sub-bands which have low-S/N, thereby resulting in higher jitter estimates. As a result, we further scrutinise the Band 3 data for further insights on the nature of jitter.

3.4. Intra-band frequency dependence of Jitter

In Section 3.3, we have demonstrated that the jitter estimates at low frequency may be affected by scintillation. This prompted us

to look at the sub-banded data to get additional insight into the nature of jitter in the different frequency channels of Band 3. In this analysis, we estimate EQUAD for each sub-band using Model II and III from the 20 highest S/N epochs listed in Table 1. EQUAD is used to account for the unaccounted (besides telescope noise) noise in the TOA uncertainty, and it corresponds to the jitter amplitude estimated using the traditional method described in the beginning of Section 3 (S14; P21).

Learning from our experience in Section 3.3, where low S/N hindered us from getting accurate jitter estimates at Band 3, we obtain credible EQUAD values by first calculating the sub-banded S/N and then adopting EQUAD values from only those high S/N observations that lie above a given threshold. The sub-banded S/N is defined as follows:

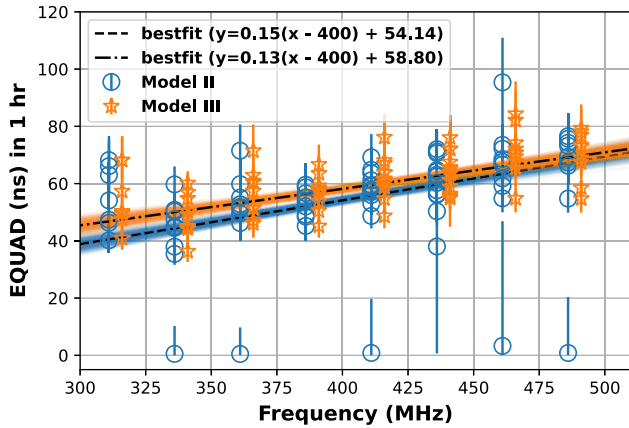$$S/N_{sub} = \frac{\sum_{i,j} I_{i,j}}{\sigma_I}, \qquad (7)$$

Figure 7. Sub-banded EQUAD scaled to one hour obtained from Model II and III estimation for the sub-bands which had the S/N_{sub} above the threshold value. The blue circles and orange stars represent the sub-banded EQUAD value of Model II (with EFAC) and III (without EFAC), respectively. The orange stars have been offset by 5 MHz to the right for clarity. The blue and orange shaded lines are from 500 random lines obtained from the posterior distribution of Bayesian regression. The reduced χ^2 of the best-fit lines are equal to 4.8 for Model II and 1.7 for Model III.

where $I_{i,j}$ is the intensity of ith phase bin and jth sub-integration in a certain sub-band, $\sigma_I = \sqrt{\sum_i \sigma_{I,i}^2}$ is the rms of the intensity in a certain sub-band, and $\sigma_{I,i}$ is the rms of the intensity in the ith phase bin. We used the median value of the S/N_sub as our threshold, which is equal to S/N_sub = 2 606.

The results from parameter estimation for Model II and III are shown in Fig. 7, which clearly show a tendency for an increase in EQUAD with frequency for both the models. To reaffirm this quantitatively, we performed a Bayesian regression and estimated the slope (a), and EQUAD at 400 MHz (Q_{400}) using the `emcee`[h] MCMC sampler (Foreman-Mackey et al. 2013). The emcee package uses an affine invariant Affine Invariant Markov chain Monte Carlo Ensemble sampler using the algorithm in Goodman &Weare (2010). We used the following regression model:

$$y = a(f - 400) + Q_{400} \qquad (8)$$

where f is the frequency. After performing the regression, we randomly sampled 500 values from the posterior distribution of a and Q_{400}, and then the results using these values are depicted as the blue and orange regions in Fig. 7. We see that the lines have a positive slope implying an increase in EQUAD with frequency, a trend that is opposite to that of S14 and P21.

The posterior distributions of a and Q_{400} are shown in Figs. 8 and 9, respectively. These plots show that the slopes have a positive value with significance of about 15σ. The plots also list the value of Q_{400}, or the jitter amplitude at 400 MHz, which is about $54.14^{+0.66}_{-0.68}$ ns, in Model II and $58.83^{+0.63}_{-0.63}$ ns, in Model III.

3.5. Jitter and the DM variations

P21 raised the concern of the jitter being the limiting factor in the DM precision measurements from shorter duration observations in all MSPs and suggested that it can only be overcome by longer integrations, based on their analysis in the high-frequency
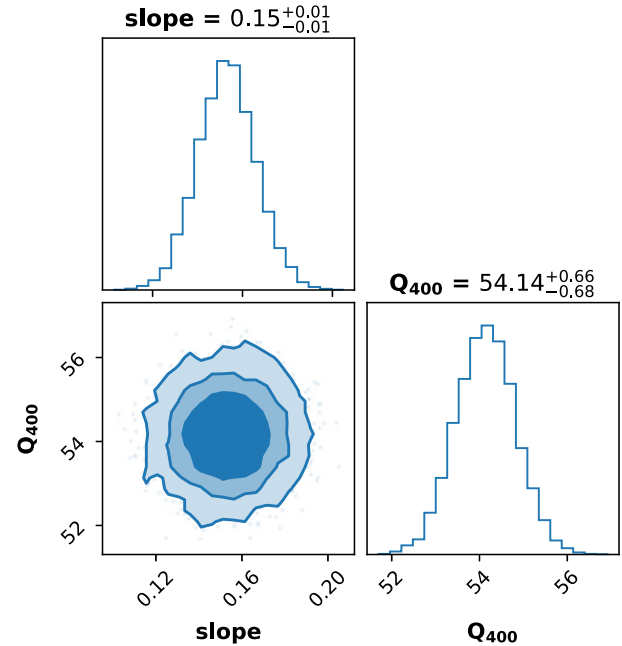
[h]https://github.com/dfm/emcee.

Figure 8. Posterior distributions with 68%, 90%, 99% credible intervals for the parameters fitted using Model II in Fig. 7. The point estimates shown above the plots represent the median values and marginalised 68 % credible intervals.
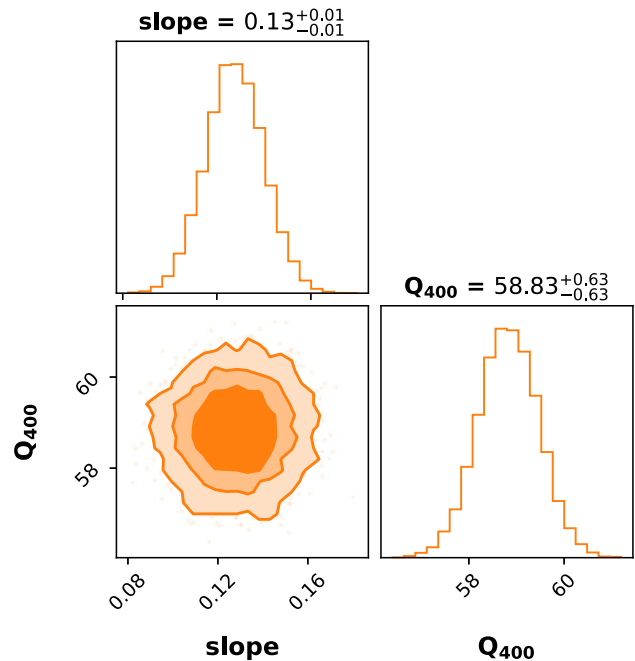

Figure 9. Posterior distributions with 68%, 90%, 99% credible intervals for the parameters fitted using Model III in Fig. 7. The point estimates shown above the plots represent the median values and marginalised 68 % credible intervals.

regime. We investigated the effect of jitter on the DM precision in the low-frequency regime (300–500 MHz) by studying the timing residuals and obtaining the DM uncertainties for 10 second sub-integrations from a 20 minute observation done at the uGMRT.
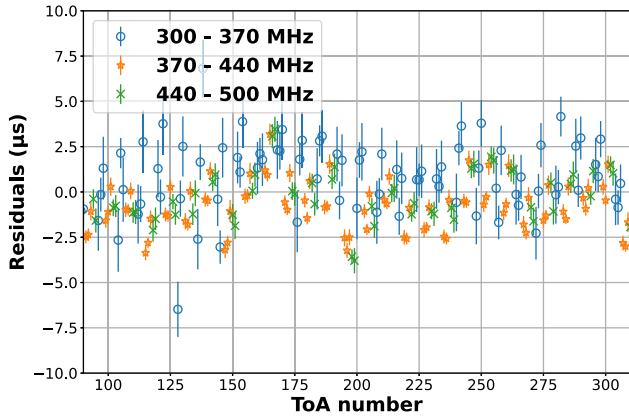
Figure 10. A subset of the 'Post-fit timing residuals' of PSR J0437−4715 estimated using 10 second sub-integrated profiles with each having eight frequency channels. The TOAs are subdivided and colour coded as three sets based on the frequency sub-band as shown in the figure. These residuals are plotted serially against the TOA numbers, to check for any potential frequency dependence and its variation for each TOA set in the plotted subset. The complete observation spanned 20 minutes, and only a subset is plotted in this figure for clarity.

Figure 11. The estimated DM values for each 10 second sub-integration from `psrfits` to the timing residuals shown in Fig. 10. The horizontal dotted line represents the median estimated DM value of 2.64386 cm^{-3} pc

We measured the timing residuals from each of its 10 second sub-integrations, where each sub-integration is divided into eight frequency channels. We plot in Fig. 10, a small subset of the post-fit timing residuals derived from the TOAs. These are plotted serially in time, with each TOA observation being 10 seconds long. The residuals are colour coded for a given frequency sub-band (as mentioned in Fig. 10). There seems to be a dependence of the timing residuals on frequency on a 10 second timescale, which may be due to the frequency dependence of DM. The dependence of the TOA on frequency at Band 3 is, however, not as strong as that shown for the high-frequency regime in P21. This probably implies a smaller spread in DM at Band 3 compared to that in the higher frequency band reported in P21.

To explore this, we measured the DM values independently from the TOAs of each 10 second sub-integration of the observation. From this, we estimated the median DM to be 2.64386 cm^{-3} pc and a standard deviation of 8.4×10^{-5}cm^{-3} pc. This is shown graphically in Fig. 11. We conclude that the scatter in DM is less at Band 3 compared to higher frequency bands (see figure 4 of P21).

Further, to understand the effect of jitter on the DM precision measurements and to get one more independent check on the DM estimation from observations alone, we use the following equation to derive the resultant error in the DM estimation:

$$\Delta t = 4.15 \times 10^6 (\text{ms}) \left(\frac{1}{f_1^2} - \frac{1}{f_2^2} \right) DM, \qquad (9)$$

where Δt is the delay in TOAs at the two observing frequencies, f_1 and f_2.

As shown in Sections 3.3 and 3.4, the pulse jitter is frequency dependent. In Band 3, it has a larger value at higher frequencies, as can be seen from Fig. 7. To estimate the contribution of pulse jitter in the DM precision, we calculate jitter for a 10 second sub-integration at the two extreme frequencies of our observation, namely 311 and 486 MHz, using Equation (2). We find the jitter estimate for a 10 second observation to be 1 121.69 and 1 287.87 ns for 311 and 486 MHz, respectively. Assuming the error in TOAs to be due to jitter alone, we infer the DM error to be
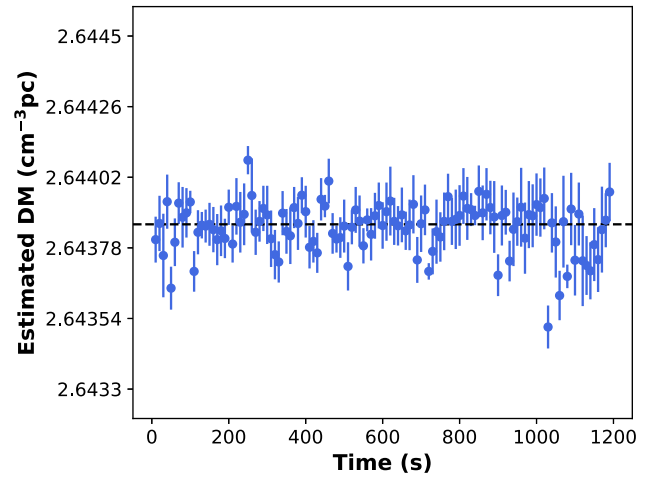
$\sim 6.7 \times 10^{-5}$cm^{-3} pc which is marginally less than our observationally derived error of $\sim 8.4 \times 10^{-5}$cm^{-3} pc. However, the error in the TOAs is not due to jitter alone and the other major factor which contributes to this error is the telescope noise. This observation on which the analysis is done is a high S/N observation, with a S/N of at least 1 000 for each 10 second sub-integration. Hence in this case, the telescope noise is about $\sim 10^{-6}$, which is slightly less than the jitter noise of $\sim 1.71 \times 10^{-6}$, and therefore, we can assert that the error in TOAs is dominated by the jitter noise in high S/N *but* lower integration time observations. Including the contribution of telescope noise in the aforementioned analysis increases the DM error marginally to be around 7.8×10^{-5}cm^{-3} pc. Thus, our two independent analyses for the DM uncertainties are in good agreement with each other, thereby providing confidence in our inferences for the jitter measurement and its effect on the DM precision.

4. Discussion

4.1. Origin of the frequency dependence in jitter

Our analysis of the high S/N Band 3 observations of PSR J0437−4715 reveals a positive correlation of jitter with frequency, as shown in Section 3.4. Therefore, we find an opposite trend than that suggested by S14 and P21 for their higher frequency observations. It could be due to two possible reasons. One is due to the possibility that the pulse profile is more stable at lower frequencies than at higher frequencies in Band 3. This is because jitter is caused by the pulse profile variation in the pulse-to-pulse scale. And second, there seems to exist a *turnover* frequency region at which the jitter trend reverses. This region seems to exist between 500 and 900 MHz, probably around 700 MHz.

The existence of a turnover frequency region at which jitter behaviour changes can possibly have two interpretations, which we outline below. The first interpretation comes from the self-absorption effect in the pulsar magnetosphere. It has been shown that the high-frequency radio emission from the pulsar comes from regions closer to its surface, while the low-frequency emission comes from regions farther from the surface (Komesaroff
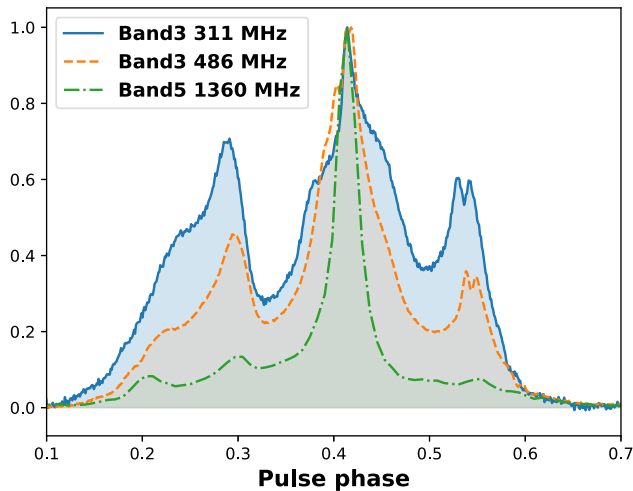
Figure 12. The integrated pulse profile of PSR J0437−4715 at different frequencies. Intensities are normalised. The data used for this plot were obtained from Cycle 41 observation on MJD 59545.

1970; Cordes 1978). This is called the radius-to-frequency mapping (RFM). Of the many pulsars studied, most show this trend but there are a few some exceptions (Posselt et al. 2021). Based on the RFM studies, we can say that since the distance of propagation through the emission region is shorter for lower frequencies, these are less sensitive to the self-absorption effects, thereby resulting in more stable profiles than those at higher frequencies. If this is true, the *turnover* frequency of the jitter amplitude could be related to the spectral *turnover* of the pulsar flux density. However, Lee et al. (2022) reported two *turnover* frequencies of the flux density for PSR J0437−4715, which are ∼285 MHz and ∼1 900 MHz. This is therefore, not supporting our *ansatz* for the change in the jitter trend. In any case, it remains to be seen how jitter behaves around these two frequencies. A holistic mapping of the jitter trend over the full span of frequency bands will probably provide a clearer picture.

The second possibility comes from the profile evolution studies. The analysis in S14 and P21 suggested that the possible reason for the smaller jitter at higher frequencies is due to narrower pulses and the larger modulation of the main pulse component at those frequencies. However, our jitter trend is opposite to their results. PSR J0437−4715 seems to have a narrow central component in its profile above 700 MHz (Dai et al. 2015). Comparing 1 400 MHz observations with 327 MHz observations for this pulsar, we find relatively more stable precursor and postcursor components at lower frequency (Osłowski et al. 2014; Vivekanand et al. 1998). We notice that the pulse profiles show more significant precursor and postcursor components in our Band 3 observations as well (see Fig. 12). This leads us to posit that the reason for the smaller jitter at lower frequencies at Band 3 is due to the fact that these precursor and postcursor components are more stable, and hence they moderate the fluctuations in the TOAs by the central (main) component. To investigate this further we need to study the phase-resolved modulation index of single pulses, which may help resolve this issue. Hence, it will be worth revisiting single-pulse studies of PSR J0437−4715 with our high-sensitivity, wideband observations, which will be defered to a future paper.

4.2. Effect of jitter on the DM precision measurements

From our analysis, in Section 3.5, we see that the DM precision is limited by jitter noise for high S/N observations on short timescales. Further, if we extrapolate the results from P21, it would indicate that we cannot get high precision DM just by going to lower frequencies. However, our analysis suggests otherwise, and it might be possible to get even better precision DMs by going to lower frequencies (∼100 MHz). Though the possibility of low frequency giving better DM precision is supported by our analysis at Band 3, it remains to be seen observationally what trend is followed by pulse jitter at that frequency regime.

Further, our analysis in tandem with P21 suggests that it is not possible to get DM precision measurements using observations at *two* (high and low) frequencies only. This is because the DM will depend on the jitter coming from both the observed frequencies; and it is entirely possible that those two frequencies may show entirely opposite trends in jitter (e.g. at Band 3 and Band 5). For more precise estimates of jitter, we need to be able to extrapolate over multiple bands in a frequency resolved manner, since different frequency bands are likely to give different estimate for order of precision.

A comprehensive understanding of the pulse-jitter behaviour over different frequency bands and its effect on DM is warranted for better precision pulsar timing. It also remains to be seen what trend in jitter is followed by different pulsars at different frequency bands. Our data show lower jitter and hence more precise DMs at lower frequencies (than higher frequencies). However, low-frequency studies of other pulsars are required to see if this trend is universal. It is very well possible that the trend is opposite for other pulsars and this is a subject of a subsequent analysis.

5. Conclusions

In this work, we present the first ever jitter measurements of PSR J0437−4715 in the low-frequency region (300–500 MHz), using Band 3 wideband observations obtained as a part of the InPTA experiment. We were able to estimate the jitter values in both Band 3 and 5 using Bayesian inference. For Band 5, our jitter measurements are in agreement with the previous studies; (S14 and P21). In this band, we estimate the weighted average of jitter to be 56.2 ± 1.6 ns. Our Band 3 weighted average value for the jitter is 53.2 ± 0.9 ns, which is lower than that in Band 5. Therefore, we see a positive correlation in the frequency dependence of jitter at low frequencies in the 300–500 MHz range. To explore the reason for this, we measured the jitter amplitude in each frequency sub-band also, using sub-banded TOAs from Band 3 observations. The results from the sub-banded data reaffirmed the positive correlation of the jitter amplitude with frequency. Therefore, positive correlation of the jitter with frequency in our low-frequency (Band 3) analysis in tandem with the negative correlation of jitter with frequency in high-frequency analysis by S14 and P21 suggests the existence of a *turnover* frequency region for the jitter amplitude. This *turnover* region probably lies somewhere between 500 and 700 MHz and this explains why our jitter amplitude of Band 3 is not as large as expected from previous high-frequency studies alone. It would be interesting to explore this *turnover* region further and this *turnover* frequency could possibly be determined by the uGMRT Band 4 (550–750 MHz) observations, or the next generation, high-sensitivity telescopes, such as the SKA.

We have also explored the DM measurements for short duration observations and the effect of jitter on its precision. Using two independent approaches, we analysed 10 second sub-integrations of a high S/N epoch to estimate the error in DM measurements. We found that the values inferred from the observational data alone are in good agreement with the analysis done using quasi-theoretical approach, using the estimated jitter values for this pulsar. We conclude that for high S/N *but* short duration observations, jitter is the dominant source of noise and limits the DM precision which for this pulsar is around 10^{-5}.

Our interesting results were achieved thanks to the high sensitivity of the uGMRT Band 3 observations. Previous studies have shown that lower frequencies suffer more from jitter noise, but our results suggest otherwise. This may, however, not always be the case. For J0437−4715, the jitter amplitude in Band 3 is about the same as in 1 400 MHz, which shows that observations at low frequency are not severely affected by the jitter noise, and we may be able obtain more stable TOAs from observations at frequencies below 300 MHz. Also, low-frequency jitter studies of other pulsars are needed for making any conclusive statements on the generic jitter behaviour for pulsars on the whole. Further, for a detailed look into the reason for this opposite trend in jitter, single-pulse analysis would be of immense help. Our future studies will provide single-pulse analysis of PSR J0437−4715 and other bright pulsars, as well as comprehensive jitter measurements of the whole InPTA pulsar set, which is important for future timing observation strategies for all PTAs.

References

Ables, J. G., McConnell, D., Deshpande, A. A., & Vivekanand, M. 1997, ApJ, 475, L33

Agazie, G., et al. 2023a, ApJ, 951, L10

Agazie, G., et al. 2023b, ApJ, 951, L8

Antoniadis, J., et al. 2023a, A&A, 678, A49.

Antoniadis, J., et al. 2023b, A&A, 678, A50

Arzoumanian, Z., et al. 2015, ApJ, 813, 65

Bailes, M., et al. 2020, PASA, 37, e028

Boynton, P. E., et al. 1972, ApJ, 175, 217

Chalumeau, A., et al. 2022, MNRAS, 509, 5538

Champion, D. J., et al. 2010, ApJ, 720, L201

Cordes, J. M. 1978, ApJ, 222, 1006

Cordes, J. M. 1980, ApJ, 237, 216

Dai, S., et al. 2015, MNRAS, 449, 3223

De, K., & Gupta, Y. 2016, ExA, 41, 67

De, K., Gupta, Y., & Sharma, P. 2016, ApJ, 833, L10

Edwards, R. T., Hobbs, G. B., & Manchester, R. N. 2006, MNRAS, 372, 1549

Ellis, J., & van Haasteren, R. 2017, jellis18/PTMCMCSampler: Official Release, doi: 10.5281/zenodo.1037579

Ellis, J. A., Vallisneri, M., Taylor, S. R., & Baker, P. T. 2020, ENTERPRISE: Enhanced Numerical Toolbox Enabling a Robust PulsaR Inference SuitE, Zenodo, doi: 10.5281/zenodo.4059815

Foreman-Mackey, D., Hogg, D. W., Lang, D., & Goodman, J. 2013, PASP, 125, 306

Foster, R. S., & Backer, D. C. 1990, ApJ, 361, 300

Goodman, J., & Weare, J. 2010, CoAMCS, 5, 65

Gupta, Y., et al. 2017, CSci, 113, 707

Hobbs, G. 2013, CQG, 30, 224007

Hobbs, G. B., Edwards, R. T., & Manchester, R. N. 2006, MNRAS, 369, 655

Hotan, A. W., van Straten, W., & Manchester, R. N. 2004, PASA, 21, 302

Jenet, F. A., Anderson, S. B., Kaspi, V. M., Prince, T. A., & Unwin, S. C. 1998, ApJ, 498, 365

Johnston, S., et al. 1993, Natur, 361, 613

Joshi, B. C., et al. 2018, JApA, 39, 51

Joshi, B. C., et al. 2022, JApA, 43, 98

Keith, M. J., et al. 2013, MNRAS, 429, 2161

Komesaroff, M. M. 1970, Natur, 225, 612

Kramer, M., & Champion, D. J. 2013, CQG, 30, 224009

Lam, M. T., et al. 2016, ApJ, 819, 155

Lee, C. P., et al. 2022, PASA, 39, e042

Lee, K. J. 2016, in Astronomical Society of the Pacific Conference Series, Vol. 502, Frontiers in Radio Astronomy and FAST Early Sciences Symposium 2015, ed. L. Qain, & D. Li, 19

Lentati, L., et al. 2014, MNRAS, 437, 3004

Liu, K., et al. 2012, MNRAS, 420, 361

Maan, Y., van Leeuwen, J., & Vohl, D. 2021, A&A, 650, A80

Manchester, R. N., et al. 2013, PASA, 30, e017

McLaughlin, M. A. 2013, CQG, 30, 224008

Osłowski, S., van Straten, W., Hobbs, G. B., Bailes, M., & Demorest, P. 2011, MNRAS, 418, 1258

Osłowski, S., van Straten, W., Hobbs, G. B., Bailes, M. Jameson, A., & Hobbs, G. 2014, Monthly Notices of the Royal Astronomical Society, 441, 3148

Parthasarathy, A., et al. 2021, MNRAS, 502, 407

Posselt, B., et al. 2021, MNRAS, 508, 4249

Reardon, D. J., et al. 2023a, ApJ, 951, L6

Reardon, D. J., et al. 2023b, ApJ, 951, L7

Shannon, R. M., & Cordes, J. M. 2010, ApJ, 725, 1607

Shannon, R. M., & Cordes, J. M. 2012, ApJ, 761, 64

Shannon, R. M., et al. 2014, MNRAS, 443, 1463

Spiewak, R., et al. 2022, PASA, 39, e027

Srivastava, A., et al. 2023, PhRvD, 108, 023008

Susobhanan, A., et al. 2021, PASA, 38, e017

Tarafdar, P., et al. 2022, PASA, 39, e053

van Haasteren, R., & Vallisneri, M. 2014, PhRvD, 90, 104012

van Straten, W., & Bailes, M. 2011, PASA, 28, 1

van Straten, W., Demorest, P., & Oslowski, S. 2012, ART, 9, 237

Vivekanand, M. 2000, ApJ, 543, 979

Vivekanand, M., Ables, J. G., & McConnell, D. 1998, ApJ, 501, 823

Xu, H., et al. 2023, RAA, 23, 075024